Fatigue crack initiation behaviors throughout friction stir welded joints in AA7075-T6 in ultrasonic fatigue

Chao He, Yongjie Liu, Jiangfeng Dong, Qingyuan Wang, Danièle Wagner, Claude Bathias

Fatigue crack initiation behaviors throughout friction stir welded joints in AA7075-T6 in ultrasonic fatigue

Chao He [a,b], Yongjie Liu [a], Jiangfeng Dong [a], Qingyuan Wang [a,*], Daniele Wagner [b], Claude Bathias [b]

[a] Key Laboratory of Energy Engineering Safety and Disaster Mechanics, Ministry of Education, Sichuan University, Chengdu 610065, PR China
[b] University Paris Ouest Nanterre, LEME Laboratory, 50 Rue de Sèvres, 92410 Ville D'Avray, France

Keywords:
Very high cycle fatigue
Friction stir welding
Aluminum alloy
Fatigue crack initiation

A B S T R A C T

This paper presents the results of experimental investigation on fatigue behaviors of friction stir welded joints in AA7075-T6 with ultrasonic fatigue test system (20 kHz). Two kinds of particles, Fe-rich intermetallic compounds and Mg_2Si-based particles, governed the fatigue crack initiation. The plastic deformation and recrystallization during welding process led to the changes in particle size and micro crack occurrence between thermo-mechanically affected zone (TMAZ) and nugget zone (NZ). Therefore, the fatigue crack initiation sites leaned to be located at the TMAZ in short fatigue life, or at the NZ in very high cycle fatigue regime.

1. Introduction

Aluminum alloy 7075 is one of the strongest aluminum alloys in industrial applications of today. Its high strength to weight ratio, together with its natural aging characteristics, makes it attractive for a number of aircraft structural applications [1]. A major problem with this alloy is that it generally presents low weldability by traditional fusion welding process. The mechanical behavior is extremely sensitive to weld solidification crack, porosity, lack-of-fusion and hazardous fumes, which are inevitable involved in fusion welding process. Therefore, the applications of aluminum alloy 7075 are currently limited to the machine parts without welding. Friction stir welding (FSW) was invented at The Welding Institute of UK in 1991 as a solid-state joining technique, and it is capable of producing high-quality joints in high strength aluminum alloys [2]. This welding technique transforms metals into a plastic state at a temperature below the melting temperature of the material, and then mechanically stirs the materials together under pressure to form a high strength welded joint [3,4].

The FSW joints used for automotive or aerospace applications are mostly subject to cyclic loading, sometimes involving high frequency vibrations. Therefore, the fatigue behavior of FSW joints is a very important issue for the design of aerospace and transport structures. Several investigations have been conducted in order to have a better understanding of the fatigue failure mechanisms of crack initiation and propagation in FSW joints. It was found that the fatigue strength of the FSW weld at 10^7 cycles was lower than that of the base metal [5], but higher than that of traditional fusion welds [3,6]. Further, welding parameters [3,7,8] and surface quality [9,10] of the FSW welds exerted a significant effect on the fatigue strength of the weld, and the fatigue crack growth resistance of the nugget zone was the lowest throughout the FSW weld, due to an intergranular failure mechanism [11]. Generally, the cyclic loading probably extends beyond a million cycles in the working service of aerospace and transport structures [12,13]. However, the fatigue strength of the FSW joint in very high cycle fatigue (VHCF) range has not been experimentally investigated. The fatigue crack initiation process, which almost governs the total fatigue life for metallic materials in the VHCF [14], is unclear for the FSW joints in high strength aluminum alloy.

In this study, ultrasonic fatigue test system (20 kHz) was employed to investigate the VHCF strength of the FSW joints in high strength aluminum alloy. Moreover, the location of fatigue crack initiation site was characterized from the observation by optical microscope (OM) and scanning electron microscope (SEM), and the local fatigue strengths in different subzones of the weld were obtained with a specially designed specimen. Finally, the effect of particle on the fatigue crack initiation mechanism was discussed in the light of crystallite size in different subzones.

2. Material and experimental method

The material selected in this study was a 10-mm-thick aluminum alloy 7075-T651 in the sheet form with dimensions of 1200 × 500 mm. AA7075 is a heat treatable alloys which can be

* Corresponding author. Tel./fax: +86 02885406919.
E-mail address: wangqy@scu.edu.cn (Q. Wang).

strengthened by precipitated phase of $MgZn_2$, and it is usually used to fabricate structural components such as aircraft fuselage panels and airplane wings in aerospace industry. Details of the nominal chemical composition and mechanical properties of AA7075-T651 are depicted in Table 1 and Table 2, respectively. Prior to welding, the plates were cleaned using ethanol and brushed to eliminate the passive oxide layer on the faying surface. A welding tool with a smooth concave shoulder and a flat pin of adjustable length was employed. The diameters of the shoulder and the pin were 25 mm and 10 mm, respectively. The shoulder was oriented at an angle of 82° to the rotation axis of the tool. The rotational speed consisted of 300 rpm in the counterclockwise direction with a translation speed of 15 cm/min. The welding direction was perpendicular to the material rolling direction as shown in Fig. 1a.

The 1-mm-thick layers both at top and bottom surface of the plate were cut off after the FSW process, to avoid the stress concentration induced by flashes. The full specimen was sectioned in transverse direction with the nugget zone located in the center, and the detailed dimensions are presented in Fig. 1b. With the central portion of full specimen, the stresses keep almost the same in all subzones of the FSW weld. To evaluate the different resistance of subzones to fatigue failure, a special specimen with a semi-circular gap was designed to position the maximum stress in a local zone of the weld, due to the wave-like distribution of the applied stress along the longitudinal axis of the samples in ultrasonic fatigue. For microstructural observation, the surface of all specimens were first polished using different grades of emery paper and then subjected to electrolytic etching at 20 V for 45 s with perchloric acid/ethanol solution.

Fatigue test was carried out using ultrasonic fatigue machine (USF-2000, Shimadzu) at a resonance frequency of 20 kHz up to a limit of 10^9 cycles. Tension–compression loading with a stress ratio of $R = -1$ was applied to the specimen with cooling by compressive air during fatigue testing. The fracture surface of all specimens was measured by SEM and OM to reveal the fatigue crack initiation and propagation mechanisms.

3. Results and discussions

3.1. Macro/microstructure and hardness

Micrographs showing different regions of the weld for AA 7075 are shown in Fig. 2. The microstructure of the welds consisted of a nugget zone (NZ), a thermo-mechanically affected zone (TMAZ) and a heat affected zone (HAZ). The weld nugget is wider at the top of the weld due to the upper surface contact with the tool shoulder. The grain structure within the nugget is fine and equiaxed and the grain size (2–7 μm) is significantly smaller than in the parent material due to the higher temperature and extensive plastic deformation. The transition region between the HAZ and the nugget was much smaller on the advancing side than on the retreating side. The grain structure within the TMAZ is elongated and deformed in an upward flowing patter around the NZ due to the mechanical action from the welding tool. The HAZ is mechanically unaffected by the welding tool, and retains the same grain structure as the base material (BM). Generally, the microstructure had significant effect on mechanical properties for metallic materials, so inhomogeneous fatigue resistance across the welds can be inferred from the microstructural changes in various zones.

Table 1
Chemical composition of 7075-T651 aluminum alloy (wt.%).

Zn	Cu	Mg	Fe	Si	Mn	Ti	Cr	Al
5.5	1.3	2.4	0.5	0.4	0.4	0.2	0.2	Balance

Table 2
Mechanical properties of 7075-T651 aluminum alloys.

As received	Ultimate strength (MPa)	Yield strength (MPa)	Modulus of elasticity (GPa)	Poison ratio	Elongation (%)
T651	462.3	435.7	72	0.33	13.2

Microhardness was measured at top and bottom region along the transverse section and the values are presented in Fig. 3. The hardness distributions of the sheet exhibit W-shaped profiles. The NZ recorded a hardness of 165 HV approximately, which is slightly lower than the BM (180 HV), but higher than the TMAZ and HAZ region. This is ascribe to that the dissolution of precipitate results in the softening in NZ [4], but fine and equiaxed grains bring the increase of hardness according to Hall–Petch equation. With conducting the test indentation far away from the middle region, the hardness value firstly decreases and then increases to that of the BM. In TMAZ, the intensive plastic deformation improves the hardness according to strain hardening, so the hardness of TMAZ increases gradually toward the center of the weld, and reaches the maximum (170 HV) at the boundary between NZ and TMAZ. The TMAZ on the retreating side (TMAZ-RS) is wider than on the advancing side (TMAZ-AS) in accordance with the microstructural observation. The minimum hardness across the welds (135 HV) is found to be located in the HAZ adjacent to the TMAZ, because the softening in HAZ is mainly attributed to the coarsening of the precipitates due to the thermal history.

3.2. S–N curves

The *S–N* results of the full FSW specimen in the range of 10^5–10^9 cycles are shown in Fig. 4, in which the fatigue strength of AA 7075 base material obtained by Wang et al. [15] are also presented for comparison. The specimens that did not fail after 10^9 cycles are plotted with arrows. It can be noted that the fatigue strength of the FSW joint decreased significantly compared with base material. At the fatigue life of 10^9 cycles, the fatigue resistance is about 70 MPa for the FSW, which accounts for only 35% of base material (200 MPa). It has been found that fatigue life of the FSW samples was always lower than that of the BM [16], but the FSW joint have a better fatigue strength than that of traditional fusion welds, because the successful FSW welds contains no inherent defects or internal flaws that are susceptible to fatigue crack initiation. But in this test, the experimental results show that the degradation of fatigue strength in high cycle fatigue and VHCF range is much more serious as compared to that in low cycle fatigue, and the defect-free FSW joint did not bring apparent improvements on fatigue performance, especially in the VHCF. Moreover, the profile of the *S–N* curve for the FSW specimen exhibits a horizontal platform in the range of 10^7–10^8 cycles and shows a step-like mode. It can be deduced that the discontinuous evolution of fatigue strength was ascribe to different fatigue failure mechanisms, and this will be discussed in the following sections.

Let us consider the effect of microstructural heterogeneity in the FSW joint on the fatigue strength. The *S–N* diagrams of different subzones across the FSW joint (the NZ, TMAZ-AS, TMAZ-RS and HAZ) are plotted in Fig. 5. Although the scatter is large, a breakpoint could be observed for all the subzone specimens to differentiate variation features of fatigue strength between high cycle fatigue and VHCF ranges, so the evolution of *S–N* curves are represented approximately with two segments of straight line, as plotted in Fig. 5. It shows that the fatigue strength of the NZ and HAZ keeps decreasing with the increasing the fatigue life up to 10^9 cycles, which the HAZ shows the highest fatigue performance

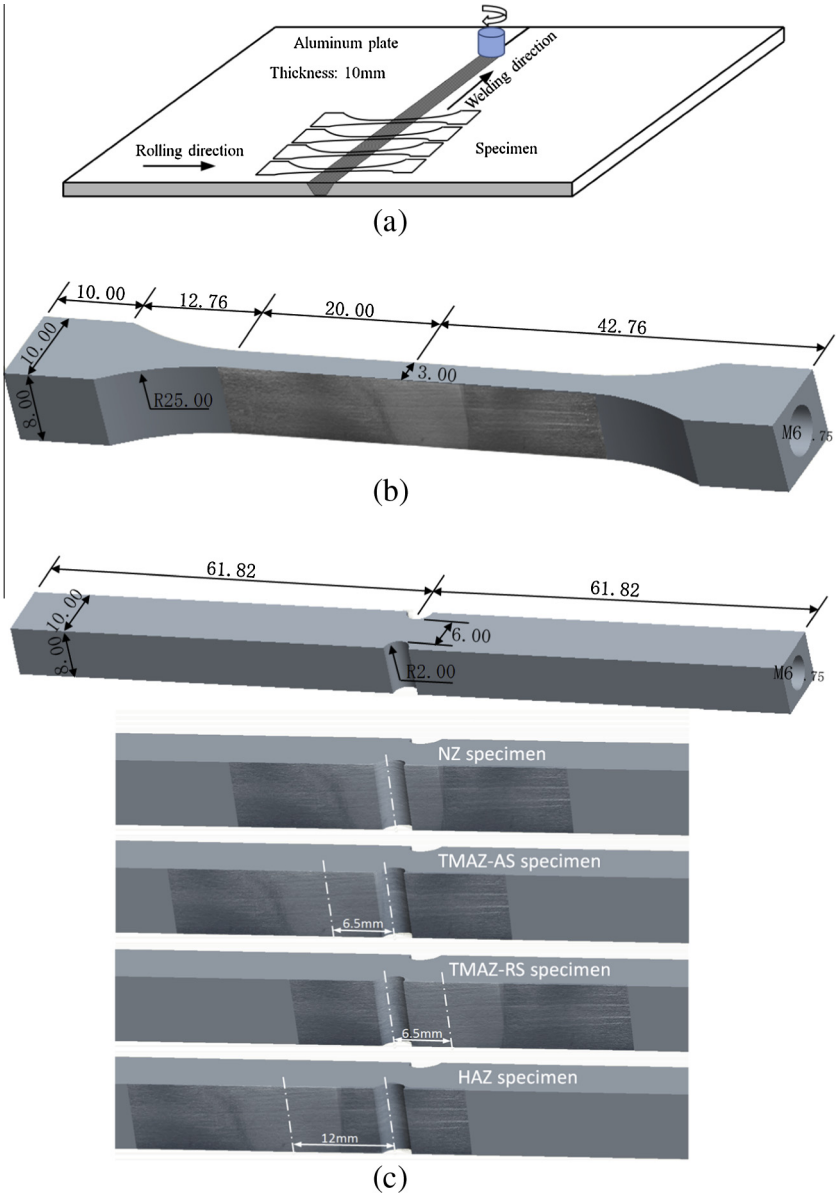

Fig. 1. Specimen design of the FSW joint in this test. (a) Location of full specimens on the FSW jointed plate; (b) dimensions of full specimen in ultrasonic fatigue test; (c) schematic illustration of the subzone specimens across the weld.

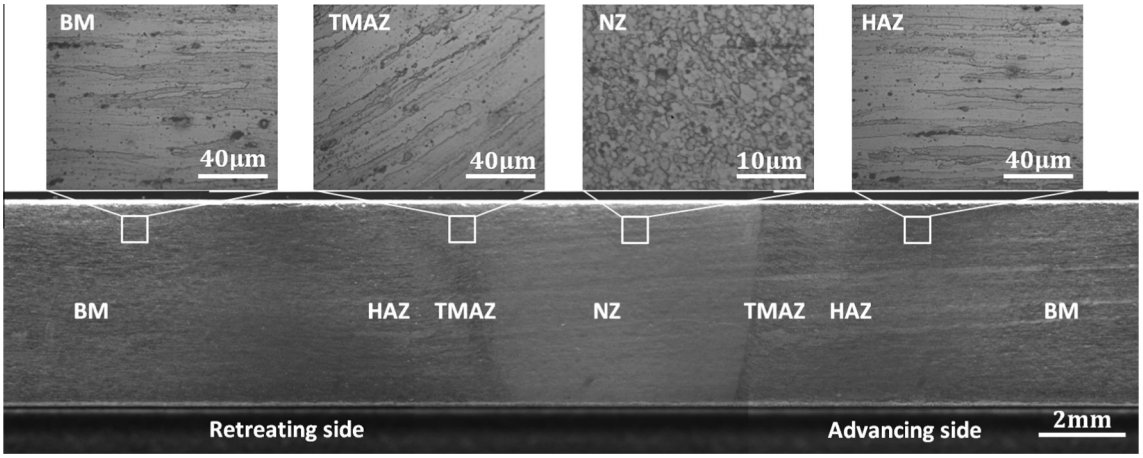

Fig. 2. Metallographic cross-section of the FSW weld.

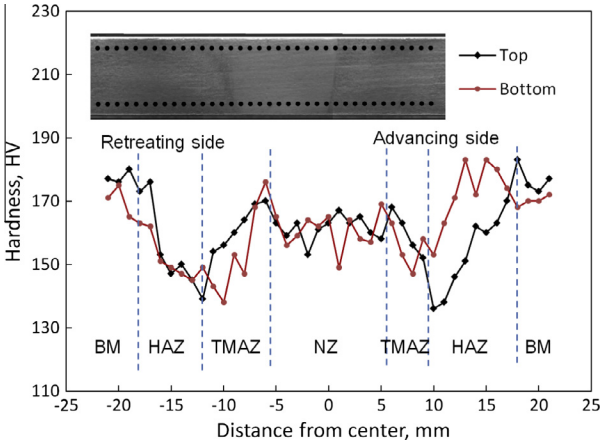

Fig. 3. Hardness transverse to weld at the top and bottom of FSW joint.

among all the subzone specimens. According to the some previous works [17,18], the HAZ of FSW aluminum alloy exhibited lower fatigue crack growth rates and higher fatigue crack growth threshold, compared to the other subzones. It seems that the softening induced by high temperature experience has limited effects on the fatigue behaviors of the HAZ, because the applied maximum stress in ultrasonic fatigue test is generally much lower than the yield strength of the HAZ. This was also confirmed in another work that the HAZ of aluminum welded joint is the weakest zone in tension test because of the softening, in spite of that, fatigue crack was prone to initiated from the defects at the fusion zone in the HCF and VHCF [19]. Therefore, the HAZ has a better fatigue strength than the NZ in the VHCF range. In addition, Fig. 5 presents that the *S–N* curves of the TMAZ exhibit a horizontal platform both in the advancing side and retreating side, so fatigue limit exists for TMAZ in the VHCF range, and the TMAZ-AS has the lower fatigue strength than that in retreating side. The differences in fatigue strength between TMAZ-AS and TMAZ-RS may be ascribe to the microstructure, of which the advancing side is characterized by a sharp boundary between the NZ and TMAZ, while the boundary in the retreating side is not clear.

3.3. Fracture surface observation

For full specimen, the location of the fatigue crack initiation site was determined by comparing the observation on both fracture surface by SEM and outside surface by OM, and the results for each

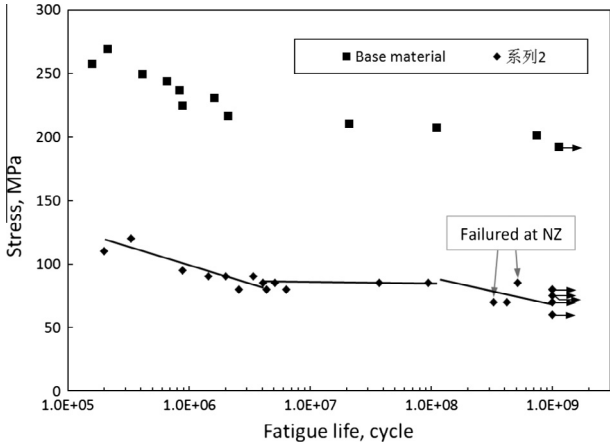

Fig. 4. Fatigue data of base material and FSW joint with full specimen.

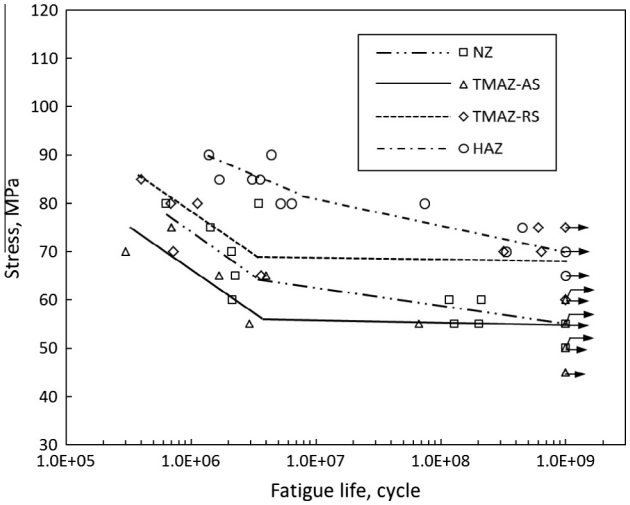

Fig. 5. Local fatigue data of FSW joint obtained from subzone specimens.

specimen are listed in Table 3. From 16 failed full specimens in this test, 14 failed at the TMAZ on the advancing side and 2 at the NZ.

If the specimen failed at the TMAZ, the typical example of the fatigue crack initiation site was shown in Fig. 6. Fig. 6a shows that the critical fatigue crack was initiated from the surface. The detailed view of the crack initiation site is shown in Fig. 6b, where a particle with a maximum length of 15 μm can be observed at the surface. The crack path on the side surface of this specimen is also presented in Fig. 6c. It can be noted that the crack length at the TMAZ is much shorter than that at the NZ after the fatigue test, which indicates that the TMAZ has a better fatigue crack growth resistance in comparison with the NZ. This is consistent with the results of fatigue crack propagation test that the crack propagation rate across the FSW welds increases once in the weld nugget [20]. Moreover, the enlarged view of the crack initiation site with OM indicated that the critical particle that inducing the crack is located at the border of the TMAZ-AS, which is adjacent to the NZ with a distance of about 90 μm.

The fatigue failure occurred at the NZ was obtained only in the VHCF range as plotted in Fig. 4. In this case, it was found that the fatigue crack initiation site of one specimen was located at the surface and another one at the subsurface. The fracture morphology of the specimen with subsurface initiation site is shown in Fig. 7. It can be seen that the fracture surface at the NZ is more flat than that

Table 3
Tested results of fatigue crack initiation sites for full specimens.

No.	Stress (MPa)	Fatigue life cycles	Crack initiation location	Particle type	Max. length of particle (μm)
1	90	3.39×10^6	TMAZ-AS	Fe-rich	18
3	80	2.59×10^6	TMAZ-AS	Mg_2Si	25
4	70	3.26×10^8	NZ	Mg_2Si	10
7	80	4.38×10^6	TMAZ-AS	Fe-rich	17
9	90	2.01×10^6	TMAZ-AS	Mg_2Si	11
10	90	1.45×10^6	TMAZ-AS	Mg_2Si	15
11	85	4.07×10^6	TMAZ-AS	Fe-rich	18
12	85	5.18×10^8	NZ	Mg_2Si	12
14	85	9.42×10^7	TMAZ-AS	Fe-rich	16
15	95	8.89×10^5	TMAZ-AS	Fe-rich	22
16	110	2.00×10^5	TMAZ-AS	Mg_2Si	22
17	120	3.34×10^5	TMAZ-AS	Fe-rich	27
18	70	4.19×10^8	TMAZ-AS	Fe-rich	14
19	80	6.34×10^6	TMAZ-AS	Fe-rich	19
21	85	3.72×10^7	TMAZ-AS	Mg_2Si	17
22	85	5.12×10^6	TMAZ-AS	Fe-rich	20

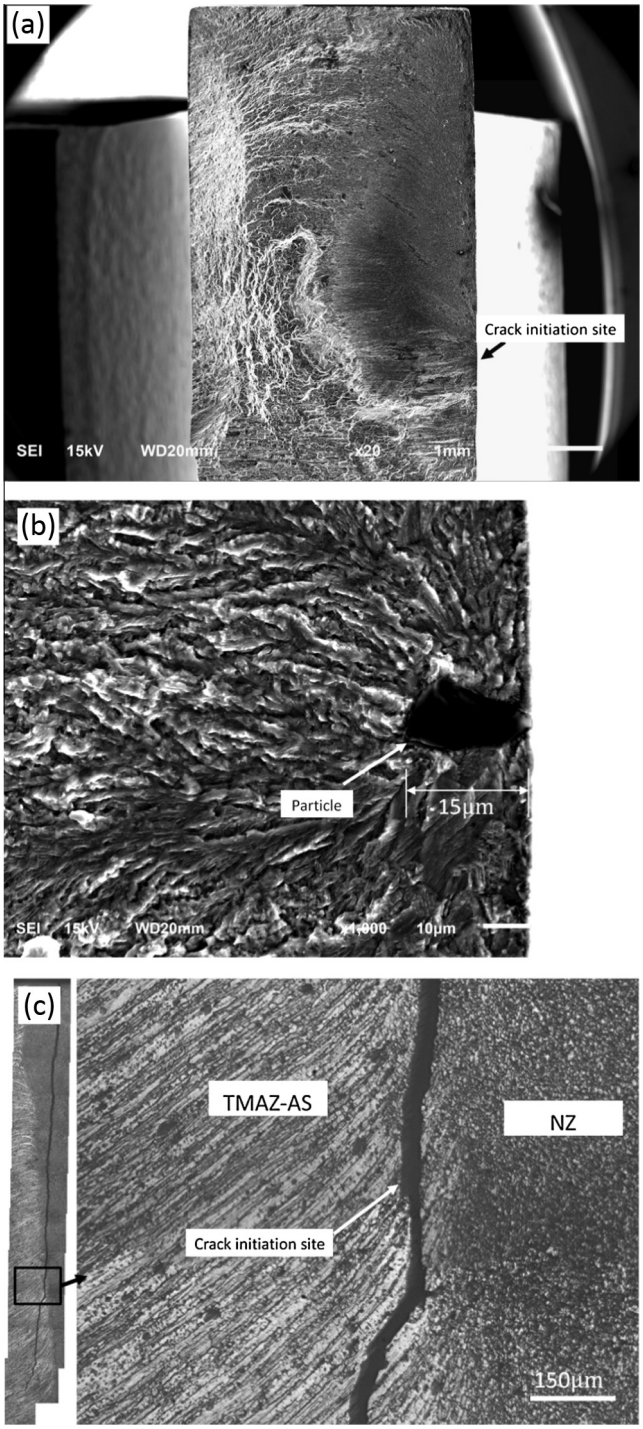

Fig. 6. SEM and OM observation of typical crack initiation site at the TMAZ-AS ($N_f = 1.45 \times 10^6$ cycles, $\sigma_b = 90$ MPa). (a) The crack initiating at the specimen surface; (b) enlargement of the fatigue crack initiation site showing a dark particle; (c) the crack locating at the TMAZ closed to the NZ.

at the TMAZ because of the generation of fine and equiaxed recrystallized grains. At the center of the initiation zone, a particle can be detected with a length of 12 μm and this is very similar to the failure mechanism of high-strength steels in the VHCF regime [21–23], which the crack initiation mostly takes place at inclusions inside the specimens and is accompanied by the formation of a ring-like fracture surface, the so-called fish-eye.

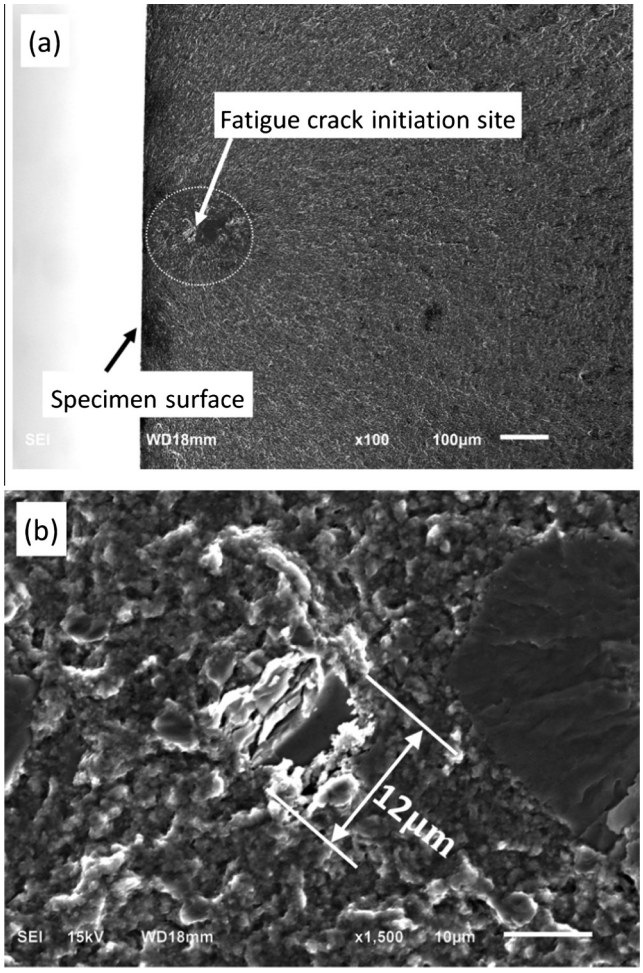

Fig. 7. Fracture morphology of a specimen failure at the NZ ($N_f = 5.18 \times 10^8$ cycles, $\sigma_b = 85$ MPa). (a) The crack location with whole morphology; (b) detail of the crack initiation site showing a particle with a diameter of 12 μm.

3.4. Fatigue crack initiation behavior

Based on results of fractographic analysis, it has been confirmed that all the fatigue cracks are initiated from the particles, regardless of where the crack are located (NZ or TMAZ). Meanwhile, it seems that the particles influence the fatigue resistance in different ways for the NZ and TMAZ, because the fatigue failure induced by particles in the NZ could only be obtained in the VHCF. In this section, discussion on fatigue crack initiation mechanisms in different subzones will be carried out with the consideration of the severe plastic deformation in the FSW process.

Fig. 8a is an electron backscatter SEM image, where two types of inclusions are presented: Fe-rich intermetallic compounds and Mg_2Si-based particles, both of which have distinguishable characteristics. The Mg_2Si particles have dark equiaxed shapes and the Fe-rich particles have gray and irregular forms. The maximum length of Fe-rich particles vary in the range of 10–25 μm and the elastic modulus is approximately 135 GPa as measured by nano-indentation [24]. The maximum size of Mg_2Si particles are about 10–20 μm *n* length, and have a modulus of approximately 50 GPa. So the Fe-rich particles are harder than the matrix of AA 7075 (72 GPa), while the Mg_2Si particles are softer. During the FSW process, the matrix embedded with particles in the TMAZ underwent intense plastic deformation, recrystallization did not

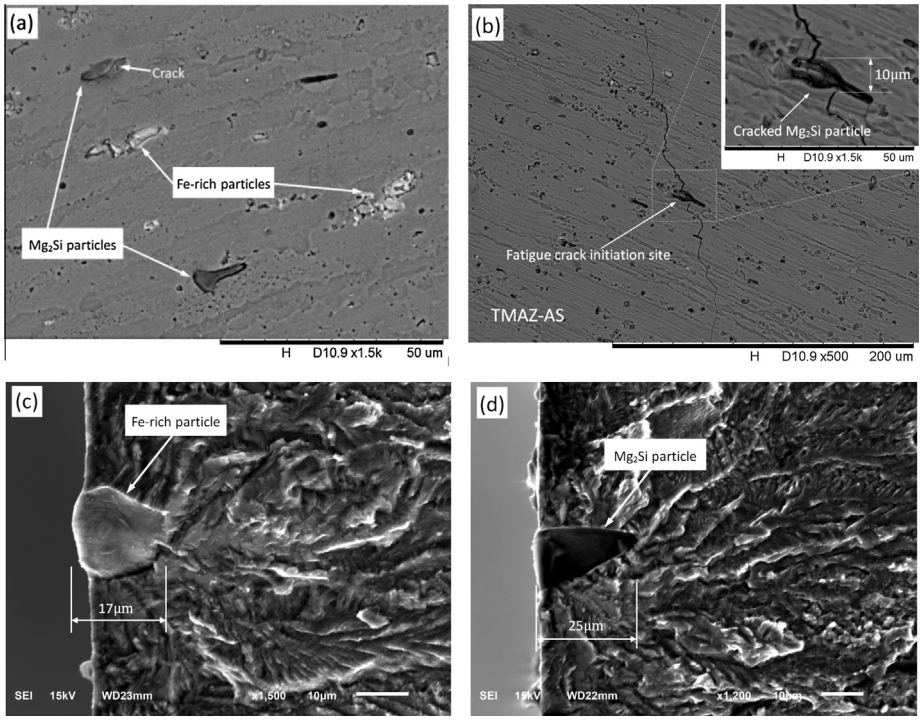

Fig. 8. Types of particles distributed at the TMAZ. (a) Morphological characteristics before the fatigue loading showing pre-existed cracks; (b) fatigue crack initiation from a cracked Mg_2Si particle (($N_f = 1.46 \times 10^6$ cycles, $\sigma_b = 90$ MPa); (c) fatigue crack initiation induced by a Fe-rich particle ($N_f = 4.38 \times 10^6$ cycles, $\sigma_b = 80$ MPa); (d) fatigue crack initiating from a Mg_2Si particle ($N_f = 2.59 \times 10^6$ cycles, $\sigma_b = 80$ MPa).

occur in this zone due to insufficient deformation strain. According to the research on the damage of aluminum alloy in tensile test [25,26], the failure process in ductile materials is associated with local failure of second phase particles. In this test, a crack within the Mg_2Si particle is also clearly observed, and the Fe-rich compounds consist of many scattered small particles as presented in Fig. 8a. It can be inferred that the intermetallic particles were crushed during the intense plastic deformation, and the cracks had already been initiated within the particles before any loading was applied, so the FSW process led to large numbers of micro cracks distributed in the TMAZ. It should be noted that the pre-existed micro cracks in the matrix seem to have limited influence on the tensile and low cycle fatigue behaviors, in which the HAZ has the lowest strength due to significantly coarsened precipitates and the development of the free precipitate zones [4]. In the VHCF, the applied stress is much lower than the yield strength, and the plastic deformation features cannot be observed even in the softest zone (HAZ). In this case, micro defects dominate the failure mechanisms for that the fatigue crack generally initiated from the defects [27,28]. During the fatigue test, the cracked particles gave rise to a crack in the surrounding matrix [29], and eventually led to the final fatigue failure as shown in Fig. 8b–d. Therefore, most of full specimens failed closed to the boundary between the TMAZ and NZ, where the elongated grains deformed most seriously in an upward flowing pattern around the NZ. As a result of that, the subzone specimens of the TMAZ on the advancing side have the lowest fatigue strength accordingly. Moreover, the cracks in the particles result in stress concentration and shorten the fatigue initiation process greatly, which is consistent with the effect of sharp notches on the VHCF behaviors of metallic materials [30]. Thus, the *S–N* curve of the TMAZ has a point of deflection at 2×10^6 cycles and a horizontal line in the VHCF range, which means a conventional fatigue limit as presented in Fig. 5.

In the NZ, intense plastic deformation and frictional heating during the FSW result in generation of a recrystallized fine-grained microstructure as shown in Fig. 9a. The particles are embedded in the matrix with a diameter of about 3–5 μm for Fe-rich particles and 6–10 μm for Mg_2Si particles, respectively, both of which are apparently smaller than that in the TMAZ. Thus, it may be thought that the cracked particles were split into many individual small particles and dispersed into the matrix separately during the dynamically recrystallization process. The pre-existed cracks formed in plastic deformation disappeared in the NZ during recrystallization process and the ability to initiate a fatigue crack was weakened accordingly. Moreover, the Mg_2Si particles in the NZ have a larger size than the Fe-rich particles, because the Fe-rich particles exhibited multiple cracks, which is much more serious than that of Mg_2Si particles [25]. Generally, the defect size is the crucial factor to control the fatigue strength in the VHCF range for high strength steel with non-metallic inclusion, and the fatigue crack initiated from the inclusion with maximum diameter [31,32]. In this test, the intergranular particles in the NZ are supposed to play similar roles as the inclusions in high strength steel for the similar failure mechanisms as presented in Fig. 7. Therefore, the Mg_2Si particle was observed to be the sole cause of fatigue crack initiation in these experiments as illustrated in Fig. 9b and c (a little blurry at the amplification of 5000× due to the capacity of SEM equipment).

As discussed above, it should be noted that the fatigue failure at the TMAZ was caused by self-cracking of particles, and fatigue cracks were initiated from the cracked particles and propagated. While in the NZ as shown in Fig. 9b and c, the fatigue crack initiation process started with the debonding between the particle and matrix instead of the self-cracking of particle. This is due to the dynamically recrystallization process, which changes the morphology of particles mainly in the following two ways:

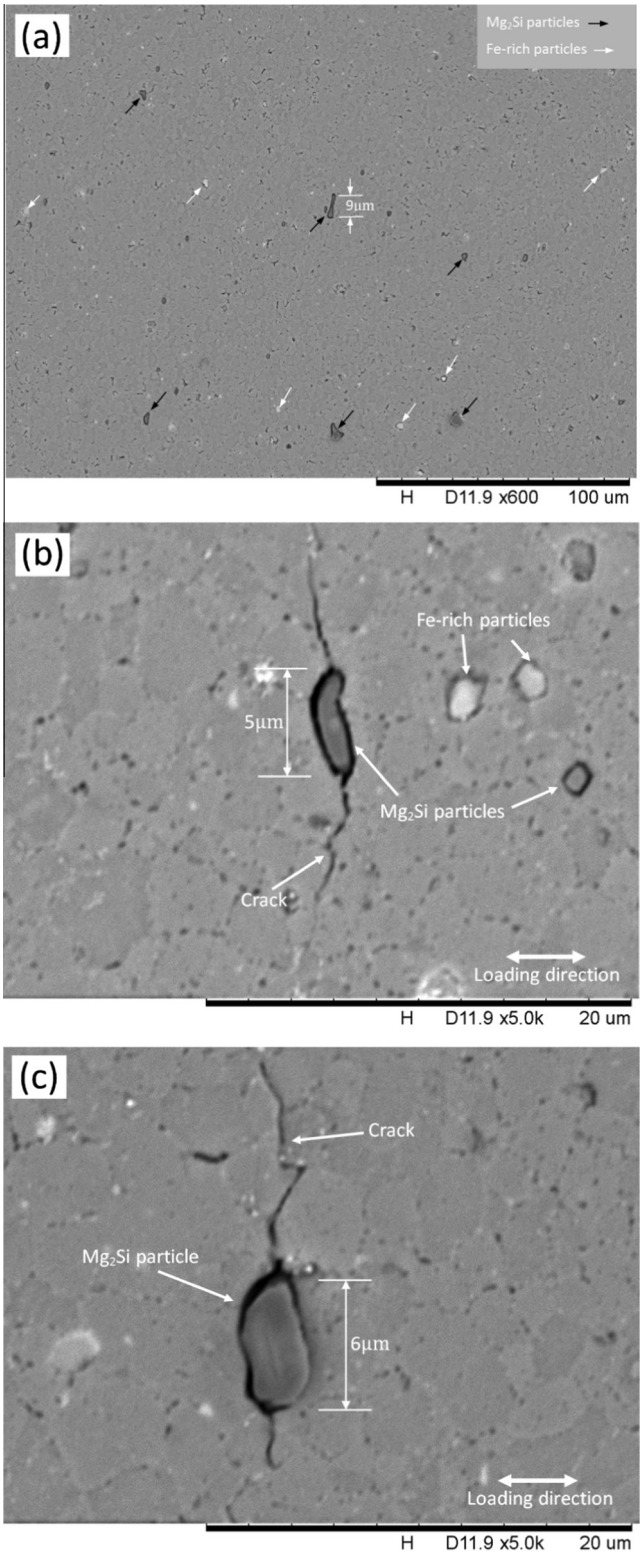

Fig. 9. Morphological characteristics of particles at the NZ. (a) Distribution and dimension features of Fe-rich and Mg_2Si particles before the fatigue test; (b) and (c) microcracks caused by the debonding between Mg_2Si particle and matrix after a loading of 3.26×10^8 cycles (70 MPa).

- Parting the cracked particles into individual smaller ones and distributing them uniformly in the NZ, so the microcracks within the particles disappeared;
- Changing the location of particles from intragranular distribution at the TMAZ to intergranular distribution at the NZ.

Therefore, the debonding nature of fatigue crack initiation in the NZ can be ascribe to the precipitate-free zones at grain boundaries of the aluminum matrix [4], which weaken the link in the microstructure. In addition, the two different fatigue crack initiation mechanisms in the TMAZ and NZ of full specimen led to the formation of the stepwise shaped *S–N* curve as shown in Fig. 4, in which the horizontal platform corresponded to the transition of fatigue failure location from the TMAZ to NZ. Furthermore, it seems that a competition of failure location between the TMAZ and NZ as the decrease of loading stress. This can also be interpreted by Fig. 9b and c, in which the specimen failed at the TMAZ, but the cracks induced by Mg_2Si particles in the NZ are confirmed. In short fatigue regime, the fatigue failure occurred at the TMAZ before the cracks at the NZ could propagate long enough to become the main fatigue crack. In the VHCF regime, the main fatigue crack was located at the NZ, because the applied stress was lower than the crack propagation threshold value of the pre-existed micro cracks at the TMAZ.

4. Conclusions

Ultrasonic fatigue test system was employed to study the very high cycle fatigue behaviors of friction stir welded joints in AA7075-T6. The local fatigue strengths in the HAZ, TMAZ and NZ were investigated, and the fatigue crack initiation mechanism was analyzed. Based on the experimental results, the following important conclusions can be drawn:

(1) For full specimens, the fatigue strength in the VHCF range accounts for only 35% of base material. The FSW joints did not show a better fatigue performance in the VHCF as comparing to traditional fusing welding. The local fatigue tests show that the TMAZ on advancing side has the lowest fatigue strengths, and a fatigue limit can be confirmed in the VHCF range.
(2) In the TMAZ, Two kinds of particles, Fe-rich intermetallic compounds and Mg_2Si-based particles, were both crushed due to the intense plastic deformation during the FSW process, resulting in the generation of micro cracks within the particles. The fatigue strength of the TMAZ decreased greatly, due to the fact that the pre-existed micro cracks shorten the fatigue crack initiation process.
(3) In the NZ, the cracked particles caused by plastic deformation were split into individual smaller ones and dispersed in the matrix, and the size of the Mg_2Si particles is larger than the Fe-rich intermetallic compounds after the dynamically recrystallization process. Accordingly, the Mg_2Si particle was the crucial sole cause of fatigue crack initiation due to debonding, because the precipitate-free zones at grain boundaries weakens the link in the microstructure.
(4) The resistances to fatigue crack initiation in the TMAZ and NZ seem to be different due to changes of particles from intragranular (TMAZ) to intergranular distribution (NZ) in the matrix. As the decrease of cyclic loading stress, the fatigue crack leaned to be originated at the TMAZ in short fatigue life, or at the NZ in very high cycle fatigue regime.

Acknowledgements

This work was financially supported by the National Natural Science Foundation of China (Grant Nos. 11327801, 11172188 and 51408382) and Fundamental Research Funds from the Central univerSities (No. 2012SCU04A05). Support of Dr. Jiukai Li and Renhui Tian is highly acknowledged.

References

[1] Rajakumar S, Muralidharan C, Balasubramanian V. Influence of friction stir welding process and tool parameters on strength properties of AA7075-T-6 aluminium alloy joints. Mater Des 2011;32(2):535–49.

[2] Thomas WM, Nicholas ED, Needham JC, Murch MG, Templesmith P, Dawes CJ. International patent application PCT/GB92/02203 and GB patent application 9125978.8; 1991.

[3] Ericsson M, Sandstrom R. Influence of welding speed on the fatigue of friction stir welds, and comparison with MIG and TIG. Int J Fatigue 2003;25(12):1379–87.

[4] Mishra RS, Ma ZY. Friction stir welding and processing. Mater Sci Eng R – Rep 2005;50(1–2):1–78.

[5] Di SS et al. Comparative study on fatigue properties between AA2024-T4 friction stir welds and base materials. Mater Sci Eng A – Struct Mater Prop Microstruct Process 2006;435:389–95.

[6] Zhou CZ, Yang XQ, Luan GH. Comparative study on fatigue properties of friction stir and MIG-pulse welded joints in 5083 Al–Mg alloy. Trans Nonferr Met Soc China 2005;15(4):789–94.

[7] Sayer S, Ceyhun V, Tezcan O. The influence of friction stir welding parameters on the mechanical properties and low cycle fatigue in AA 6063 (AlMgSi0.5) alloy. Kovove Mater-Met Mater 2008;46(3):157–64.

[8] Aydin H et al. Effect of welding parameters on tensile properties and fatigue behavior of friction stir welded 2014-T6 aluminum alloy. Trans Indian Inst Met 2012;65(1):21–30.

[9] Hatamleh O, Lyons J, Forman R. Laser peening and shot peening effects on fatigue life and surface roughness of friction stir welded 7075-T7351 aluminum. Fatigue Fract Eng Mater Struct 2007;30(2):115–30.

[10] Vidal C, Infante V. Fatigue behavior of friction stir-welded joints repaired by grinding. J Mater Eng Perform 2014;23(4):1340–9.

[11] Jata KV, Sankaran KK, Ruschau JJ. Friction-stir welding effects on microstructure and fatigue of aluminum alloy 7050-T7451. Metall Mater Trans A – Phys Metall Mater Sci 2000;31(9):2181–92.

[12] Wang QY, Li T, Zeng XG. Gigacycle fatigue behavior of high strength aluminum alloys. Fatigue 2010;2(1):65–70.

[13] Bathias C, Drouillac L, Le Francois P. How and why the fatigue S–N curve does not approach a horizontal asymptote. Int J Fatigue 2001;23:S143–51.

[14] Wang QY et al. High-cycle fatigue crack initiation and propagation behaviour of high-strength spring steel wires. Fatigue Fract Eng Mater Struct 1999;22(8):673–7.

[15] Wang QY, Kawagoishi N, Chen Q. Fatigue and fracture behaviour of structural Al-alloys up to very long life regimes. Int J Fatigue 2006;28(11):1572–6.

[16] Ceschini L et al. Effect of friction stir welding on microstructure, tensile and fatigue properties of the AA7005/10 vol.%Al_2O_3p composite. Compos Sci Technol 2007;67(3–4):605–15.

[17] Kim SJ, Jeong YH, Sohn HJ. Probabilistic fatigue crack growth in compact tension specimens from FSWed 7075-T651 aluminum alloys. Mech Eng Mater 2012;152–154:293–6. Pts 1-3.

[18] Ma YE et al. Mechanical properties and fatigue crack growth rates in friction stir welded nugget of 2198-T8 Al–Li alloy joints. Mater Sci Eng A – Struct Mater Prop Microstruct Process 2013;569:41–7.

[19] He C et al. Effects of mechanical heterogeneity on the tensile and fatigue behaviours in a laser-arc hybrid welded aluminium alloy joint. Mater Des 2015;65:289–96.

[20] Pouget G, Reynolds AP. Residual stress and microstructure effects on fatigue crack growth in AA2050 friction stir welds. Int J Fatigue 2008;30(3):463–72.

[21] Hong YS et al. Propensities of crack interior initiation and early growth for very-high-cycle fatigue of high strength steels. Int J Fatigue 2014;58:144–51.

[22] Huang ZY et al. Subsurface crack initiation and propagation mechanisms in gigacycle fatigue. Acta Mater 2010;58(18):6046–54.

[23] Marines-Garcia I et al. Fatigue crack growth from small to large cracks on very high cycle fatigue with fish-eye failures. Eng Fract Mech 2008;75(6):1657–65.

[24] LE O. Effects of microstructure on high-cycle fatigue of an Al–Zn–Mg–Cu Alloy (Al-7075). Masters thesis. School of Engineering, University of Pittsburgh; 2003.

[25] Lugo M et al. Quantification of damage evolution in a 7075 aluminum alloy using an acoustic emission technique. Mater Sci Eng A 2011;528(22–23):6708–14.

[26] Balasundaram A et al. Three-dimensional particle cracking damage development in an Al–Mg-base wrought alloy. Mater Sci Eng A 2003;355(1–2):368–83.

[27] He C et al. Fatigue damage evaluation of low-alloy steel welded joints in fusion zone and heat affected zone based on frequency response changes in gigacycle fatigue. Int J Fatigue 2014;61:297–303.

[28] Zhu ML et al. Very high cycle fatigue behavior of a low strength welded joint at moderate temperature. Int J Fatigue 2012;40:74–83.

[29] Payne J et al. Observations of fatigue crack initiation in 7075-T651. Int J Fatigue 2010;32(2):247–55.

[30] Pyttel B, Schwerdt D, Berger C. Very high cycle fatigue – Is there a fatigue limit? Int J Fatigue 2011;33(1):49–58.

[31] Li SX. Effects of inclusions on very high cycle fatigue properties of high strength steels. Int Mater Rev 2012;57(2):92–114.

[32] Lu LT, Zhang JW, Shiozawa K. Influence of inclusion size on S–N curve characteristics of high-strength steels in the giga-cycle fatigue regime. Fatigue Fract Eng Mater Struct 2009;32(8):647–55.